

DOUBLE-PEAKED X-RAY LINES FROM THE OXYGEN/NEON-RICH ACCRETION DISK IN 4U 1626–67

NORBERT S. SCHULZ, DEEPTO CHAKRABARTY,¹ HERMAN L. MARSHALL, CLAUDE R. CANIZARES,¹
 JULIA C. LEE, AND JOHN HOUCK

Center for Space Research, Massachusetts Institute of Technology, Cambridge, MA 02139;
 nss,deepto,hermanm,crc,jlee,houck@space.mit.edu

Accepted for publication in *The Astrophysical Journal*

ABSTRACT

We report on a 39 ks observation of the 7.7-s low-mass X-ray binary pulsar 4U 1626–67 with the High Energy Transmission Grating Spectrometer (HETGS) on the *Chandra X-Ray Observatory*. This ultracompact system consists of a disk-accreting magnetic neutron star and a very low mass, hydrogen-depleted companion in a 42-min binary. We have resolved the previously reported Ne/O emission line complex near 1 keV into Doppler pairs of broadened (≈ 2500 km s⁻¹ FWHM) lines from highly ionized Ne and O. In most cases, the blue and red line components are of comparable strength, with blueshifts of 1550–2610 km s⁻¹ and redshifts of 770–1900 km s⁻¹. The lines appear to originate in hot ($\approx 10^6$ K), dense material just below the X-ray-heated skin of the outer Keplerian accretion disk, or else possibly in a disk wind driven from the pulsar’s magnetopause. The observed photoelectric absorption edges of Ne and O appear nearly an order of magnitude stronger than expected from interstellar material and are likely formed in cool, metal-rich material local to the source. Based on the inferred local abundance ratios, we argue that the mass donor in this binary is probably the $0.02 M_{\odot}$ chemically fractionated core of a C-O-Ne or O-Ne-Mg white dwarf which has previously crystallized.

Subject headings: accretion, accretion disks — binaries: close — stars: individual (4U 1626–67) — stars: neutron — techniques: spectroscopic — X-rays: stars

1. INTRODUCTION

The ultracompact low-mass X-ray binary 4U 1626–67 consists of a 7.7 s pulsar accreting from an extremely low-mass ($\lesssim 0.1 M_{\odot}$) companion with a binary separation of only ≈ 1 lt-sec. The very short binary period ($P_{\text{orb}}=42$ min; Middlethick et al. 1981; Chakrabarty 1998) indicates that the companion must be extremely hydrogen-poor (Paczynski & Sienkiewicz 1981; Nelson, Rappaport, & Joss 1986). Based on X-ray timing limits, the Roche-lobe-filling companion must be either a $0.02 M_{\odot}$ white dwarf or a $0.08 M_{\odot}$ hydrogen-depleted, partially degenerate star (Levine et al. 1988; Verbunt, Wijers, & Burm 1990; Chakrabarty 1998). These solutions correspond to relatively face-on binary inclinations of 33° and 8° , respectively. For a randomly oriented ensemble of binaries, the a priori probabilities of finding such low inclinations are only 16% and 1%, respectively².

The pulsar’s spin frequency evolves on short ($|\dot{\nu}/\nu| \approx 6000$ yr) time scales due to accretion torques. After spinning up steadily for 13 years, the accretion torque abruptly changed sign in 1990, leaving the pulsar in a prolonged spin-down state (Chakrabarty et al. 1997). The surface dipole magnetic field strength of 3×10^{12} G, inferred from the detection of cyclotron absorption lines (Orlandini et al. 1998), suggests that the pulsar is near spin equilibrium. The ultraviolet spectrum of the source is consistent with that of an accretion disk whose inner edge is truncated by the pulsar’s magnetosphere near the corotation radius $r_{\text{co}} = (GM_X P_{\text{spin}}^2 / 4\pi^2)^{1/3} = 6.5 \times 10^8$ cm, and whose outer edge is truncated at the binary’s tidal radius $r_t \approx 2 \times 10^{10}$ cm (Wang & Chakrabarty 2001).

The pulsar’s X-ray continuum spectrum is evidently corre-

lated with its torque state. During the 1977–1990 spin-up epoch, the pulsar’s pulse-phase-averaged X-ray spectrum was roughly described by the sum of three separate power-law components with photon indices³ $\gamma_1 \approx 1.4$ – 1.65 (0.7–10 keV), $\gamma_2 \approx 0.5$ (10–20 keV), and $\gamma_3 \approx 5$ (20–60 keV) (Pravdo et al. 1979; Maurer et al. 1982; Elsner et al. 1983; Kii et al. 1986; Mavromatakis 1994). However, observations acquired after the 1990 torque reversal measured a significantly flatter soft X-ray spectrum with $\gamma_1 \approx 0.6$ – 0.8 in the 1–10 keV range (Angelini et al. 1995; Owens et al. 1997; Vaughan & Kitamoto 1997). Since the discovery of this X-ray source over two decades ago, its overall X-ray flux has declined steadily (Chakrabarty et al. 1997 and references therein; Owens et al. 1997), but the optical flux from the accretion disk has remained essentially constant over the same time interval (Chakrabarty 1998).

X-ray spectroscopy with *ASCA* and *BeppoSAX* also detected a strong, unusual complex of emission lines near 1 keV; these were identified as the Ly α lines of hydrogenic and He-like Ne and O (Angelini et al. 1995; Owens et al. 1997), with possible contributions from Fe-*L* shell emission. Angelini et al. (1995) also detected a faint feature near 1.41 keV, which suggests the presence of photoionized plasma if the feature is interpreted as the recombination continuum of hydrogenic Ne. Independent of whether the line complex arises from a photoionized or a collisionally ionized plasma, however, its strength indicates an overabundance of both Ne and O relative to solar values (Angelini et al. 1995).

In this paper, we present high-resolution spectra of 4U 1626–67 obtained with the High Energy Transmission Grating Spectrometer (HETGS; Canizares et al. 2001, in preparation) on board the *Chandra X-ray Observatory*.

¹ Also Department of Physics, Massachusetts Institute of Technology, Cambridge, MA 02139.

² A more massive $0.6 M_{\odot}$ helium-burning star is also allowed by the X-ray timing limits (with $i = 1.3^{\circ}$ and an a priori probability of 0.03%), but this solution requires an implausible (36 kpc) distance to be consistent with the observed X-ray flux.

³ We define photon index γ such that the photon flux $dN/dE \propto E^{-\gamma}$.

2. CHANDRA OBSERVATIONS AND DATA REDUCTION

4U 1626–67 was observed with the HETGS on 2000 September 16 (05:47:21 UT) continuously for 39 ks. The HETGS carries two different types of transmission gratings: the Medium Energy Gratings (MEG) and the High Energy Gratings (HEG). These allow for high-resolution X-ray spectroscopy in the 1–35 Å (0.35–12.4 keV) range, with a spectral resolution of $\lambda/\Delta\lambda \approx 1400$ at 12 Å (1 keV) and $\lambda/\Delta\lambda \approx 180$ at 1.8 Å (6.9 keV). The dispersed spectra were recorded with an array of 6 charged coupled devices (CCDs) in the focal plane which are part of the Advanced CCD Imaging Spectrometer (ACIS; Garmire et al. 2001, in preparation). We defer to the *Chandra* X-ray Center (CXC) documents for a more detailed description of the spectroscopic instruments (see <http://chandra.harvard.edu>).

We recorded a total of 62373 events in the 1st order MEG spectrum and 33744 events in the HEG spectrum after applying standard event grade selection cuts. For some of the analysis, we combined the MEG and HEG spectra where their passbands overlapped. In these cases, we used a count-weighted average of the resolution of both gratings, which is between 0.01 and 0.02 Å. The CXC provided aspect-corrected “level 1” event lists via standard pipeline processing. These data were reprocessed using the latest available data processing input products. We also removed all events that were attributed to bad pixels, bad columns, or flaring background events that were not handled by the CXC standard processing.

The determination of the zeroth order source position is crucial for the calibration of the wavelength scales, since it defines the zero point for wavelength in the dispersed spectra. We can determine the source position on the detector to an accuracy of 0.2 pixels, which corresponds to a wavelength zero point accuracy of 0.002 Å in MEG and 0.001 Å in the HEG 1st order. The current status of the overall wavelength calibration is of order $\sim 0.05\%$, leading to a worst-case uncertainty of 0.004 Å in the 1st order MEG at O VII (21.6 Å), and 0.006 Å in the 1st order HEG at Ne X (12.1 Å). We processed the event lists into “level 1.5” grating event lists using available CXC software. For the spectral analysis we used a combination of custom software, FTOOLS, and the CIAO 2.1 package from CXC. We computed aspect-corrected exposure maps for each spectrum, allowing us to correct for effects from the effective area of the CCD spectrometer. The overall flux calibration throughout the CCD array is of order 10%, although it can be as poor as 20% at lower energies in some areas.

The zeroth order image was affected by heavy “pileup”, where the event rate was so high that two or more events were detected in the CCD during a 3.2 s frame exposure. The time between frames was $dt = 3.24104$ s, which accounts for the time to transfer charge to the frame store. Pileup distorts the CCD spectrum because detected events overlap so their deposited charges are collected into single, apparently more energetic events. More significant, however, is that many events are lost on-board as the grades of the piled events overlap those of rejected background. In this case $\sim 90\%$ of the events are lost. We ignore the zeroth order events in all subsequent analyses.

MEG and HEG events were selected for timing analysis on the basis of spatial, pulse height, and grade selection (as described in the last section). Events from first and second orders were included, giving 102,835 events. For the same pulse height and grade selection, a background region 12.6'' away

gave only 386 events in the same spatial window, so background is ignored. Event times were corrected for the motion of the spacecraft and then to the solar system barycenter. A random quantity uniformly distributed between 0 and dt was added to event times in order to avoid aliasing with the sample time. A significant peak was found in the FFT at a period of 7.672 s and a χ^2 period folding method gave a best period of 7.6717(7) s, consistent with an extrapolation of the source’s long-term spin-down behavior (Chakrabarty et al. 1997). The pulse appears sinusoidal with an amplitude of $4.0 \pm 0.9\%$, averaged over the entire bandpass. This sinusoidal appearance may as well be a consequence of the fact that the pulse period is very close to the time resolution of the detector. It has been shown in previous observations that the shape and amplitude of the intrinsic pulse change with energy (Pravdo et al. 1979, Kii et al. 1986, Owens et al. 1997). In this respect we observe that the modulation of the events with $E > 2$ keV is $5.3 \pm 1.3\%$, somewhat higher than the modulation found in the lower energy band ($E < 2$ keV): $2.7 \pm 1.2\%$. Above 2 keV, the hard power law dominates the spectrum (see section 4.2) while below 1 keV, the power law and blackbody components have about equal contributions (see Fig. 4), so this marginally significant change of the pulse fraction could be obtained if the blackbody component is totally unpulsed.

3. SPECTRAL ANALYSIS

The preparation of the spectra for analysis was done in several steps. In order to perform the basic spectral fits, we first subtracted the background from each spectrum and fitted the HEG and MEG spectra simultaneously using the XSPEC v11.0 package (Arnaud 1996). We also co-added all background-subtracted spectra and exposure maps and divided the spectra by these exposure maps in order to screen the fit against local deviations and adjust the fit. The exposure map consists of the aspect-corrected effective area of the instrument over the total exposure for each dispersion arm. The source spectra were extracted within a cross-dispersion width of 2×10^{-3} degrees encompassing 98% of the dispersed flux on the CCD. We then selected the first-order spectra from the HEG and MEG. The background spectra were computed by extracting spectra above and below the dispersed flux, again with the same total width in cross-dispersion. The background usually appeared extremely weak, although we observed some enhanced flux in the MEG -1st order range between 16 and 20 Å, at a level about a factor of 2.5 above the average. Figure 1 shows the background-subtracted count spectrum after co-adding the MEG and HEG spectra. The lower curve shows the total contributing background above 10 Å.

3.1. Photoelectric Absorption

Photoelectric absorption by neutral metals along our line of sight through the interstellar medium attenuates the low-energy X-ray continuum. With HETGS, we are able to resolve the individual photoelectric absorption edges of Ne-K (14.3 Å), Fe-L_{III} (17.5 Å), and O-K (23.3 Å), allowing separate determinations of the column density for each of these elements (see Table 1). Figure 2 shows the Ne K and Fe L-edges. We note that the uncertainties in these edges are still large, since the derived absolute edge depths are of the order of the statistical uncertainties of the data bins, and their determination therefore also depends on the proper placement of the continuum (see below).

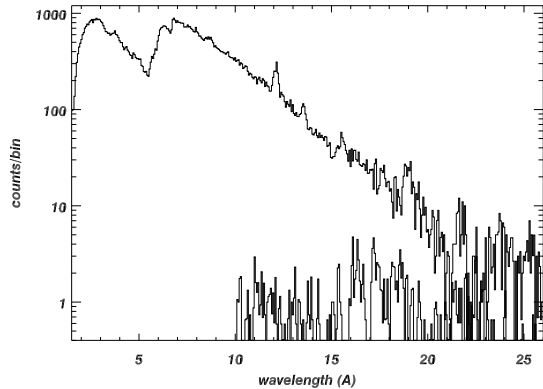


FIG. 1.— The *Chandra*/HETGS count spectrum of 4U 1626–67. The upper curve is the total background-subtracted spectrum, and the lower curve is the background above 10 Å.

For Ne and O, we used the atomic cross sections of Verner et al. (1993) but for Fe-*L* we instead used more recent laboratory atomic constants (Kortright & Kim 2000; see also discussion in Schulz et al. 2001). Also given in Table 1 is the column density of neutral hydrogen (N_{H}) implied by each element’s absorption edge, assuming the abundances of Morrison & McCammon (1983) for the material along the line of sight. It is interesting to note that for Ne and O, these implied values of N_{H} are higher than the value of $N_{\text{H}} = (6.2 \pm 0.7) \times 10^{20} \text{ cm}^{-2}$ measured directly from Ly α measurements in the ultraviolet (Wang & Chakrabarty 2001). The abundance ratios also differ substantially from solar values.

Although the threshold for the C-*K* edge (43.7 Å) lies beyond our passband, the short wavelength “tail” of this edge does affect the continuum we observe. One way to obtain a better representation of the continuum in the wavelength range above 18 Å is to assume a C/H number ratio (5–18) \times solar. For our continuum representations in the figures below, we have conservatively assumed a carbon overabundance of $(\text{C}/\text{H})/(\text{C}/\text{H})_{\odot} = 5$. Given that $N_{\text{H}} \lesssim 3 \times 10^{21} \text{ cm}^{-2}$, we expect no sensitivity to absorption edges of Mg and higher-*Z* elements. However, it is interesting to note the presence of a marginal edge-like feature near the position of the Mg *K*-edge at 9.5 Å. In order to explain this feature by Mg absorption, we would require an order of magnitude overabundance of Mg relative to the solar value.

TABLE 1
PHOTOELECTRIC ABSORPTION TOWARDS 4U 1626–67

λ (Å)	Edge	Optical Depth	Total N_{Z}^{a} (10^{17} cm^{-2})	Implied N_{H}^{b} (10^{21} cm^{-2})	Local N_{Z}^{c} (10^{17} cm^{-2})
9.5 ^d	Mg <i>K</i> (?)	0.094 \pm 0.052 ^d	3.8 \pm 2.1 ^d	9.4 \pm 5.2 ^d	3.5 \pm 2.1 ^d
14.3	Ne <i>K</i>	0.19 \pm 0.09	5.2 \pm 2.5	3.7 \pm 1.8	4.4 \pm 2.5
17.5	Fe <i>L</i> _{III}	0.25 \pm 0.11	0.35 \pm 0.16	1.1 \pm 0.5	0.15 \pm 0.15
23.3	O <i>K</i>	1.40 \pm 0.67	25 \pm 12	3.3 \pm 1.6	20 \pm 12
43.7	C <i>K</i> ^e	...	10–36 ^e	2.2–8.1 ^e	7–33 ^e

^aTotal column density for specified element.

^b N_{H} implied by total N_{Z} assuming standard ISM abundances (Morrison & McCammon 1983). For comparison, the directly measured N_{H} from Ly α is $(0.62 \pm 0.07) \times 10^{21} \text{ cm}^{-2}$.

^cColumn density local to source for specified element, after correcting for interstellar absorption using $N_{\text{H}} = 6.2 \times 10^{20} \text{ cm}^{-2}$ and standard ISM abundances.

^dFeature not reliably identified in our data.

^eEdge lies outside our bandpass. Strength is inferred indirectly from continuum strength redward of O edge.

3.2. Continuum Model and Fluxes

To fit the continuum spectrum, we rebinned the data into broad (0.08 Å) bins, resulting in about 300 wavelength channels. To avoid skewing of the fit due to obvious bright lines, we always included several Gaussian line components in the model fit. This task appeared to be quite difficult, since we observe quite a number of lines (see below) in the spectrum, which appear very broad and a substantial uncertainty remains due to the fact that we cannot identify possible contributions from many more weak broad lines. Spectral models with a single absorbed continuum component did not fit the data. However, absorbed two-component fits were successful using either a pair of power-law components or a sum of power-law and blackbody components. The best-fit parameters are given in Table 2. Although the HETGS data does not clearly prefer one model over the other, the PL+BB model is consistent with previous low-resolution broadband measurements (Angelini et al. 1995, Owens et al. 1997), and we will adopt this model with the photon index fixed at 0.65 for the remainder of this paper. The spectrum versus wavelength is shown in Figure 3. A plot of the photon spectrum versus energy is shown in Figure 4, with the individual continuum components clearly indicated.

The total measured X-ray flux is $2.09 \times 10^{-10} \text{ erg cm}^{-2} \text{ s}^{-1}$ (0.5–10 keV). This corresponds to an (unabsorbed) luminosity of $2.6 \times 10^{34} \text{ erg s}^{-1} d_{kpc}^2$, which is similar to that reported by Owens et al. (1997). This would seem to break the trend of steady dimming over the entire source history (Chakrabarty et al. 1997). The blackbody temperature is also consistent with that measured by Owens et al. (1997).

3.3. Emission Lines

In order to study discrete line features, we subtracted the continuum model from the measured photon spectrum. This residual spectrum is shown at the bottom of Figure 3. It shows a variety of emission and absorption features. We have chosen not to analyze the wavelength range below 8 Å, since the possible features are weak and are not easily disentangled from calibration uncertainties. The residual spectrum contains several strong emission line features at higher wavelength, which we identify exclusively from hydrogenic and He-like Ne and O ions. Fitting single Gaussians to the lines yielded line widths ranging from 0.25 Å at Ne X to 0.48 Å at O VII, corresponding to Doppler velocities of 5340 and 7460 km s^{-1} , respectively. The centroid of the Ne IX lines is closest to the expected position of the intercombination line, while the O VII line lies between the expected positions for the intercombination and resonance lines.

Single Gaussian line profiles did not provide an acceptable fit to the observed line shapes. Figure 5 shows the profiles of the neon and oxygen lines, using spectral binnings of 0.015 Å and 0.06 Å. The H-like lines clearly show a double line profile. We therefore fit all observed line profiles with Gaussian line doublets. The resulting line parameters are given in Table 3. For the He-like triplet lines, we assumed that the individual components of each triplet were subject to the same velocity shift, and we also enforced an upper limit on the line flux using the 3σ error level of the continuum. We also can further set a lower limit for these fluxes from calculations for photoionized plasmas by Porquet and Dubau (2000); specifically, the lines of both Ne IX and O VII should obey $G \lesssim 4.9$ (see below).

For each line pair, we denote the higher and lower wave-

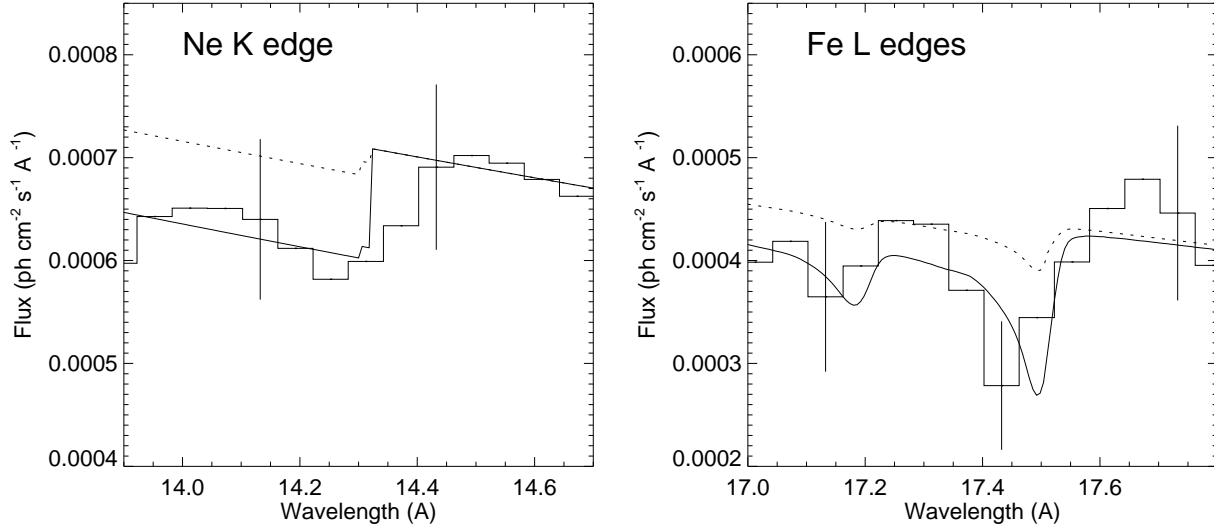


FIG. 2.— The spectrum of 4U 1626–67 near the Ne *K*-edge (*left*) and the Fe *L*-edges (*right*). The data have been smoothed for illustrative purposes. The dotted lines show the expected contribution of interstellar photoelectric absorption based on an ultraviolet measurement of N_{H} . The solid lines show the best-fit model for the much stronger absorption edges in the *Chandra* data.

length components as “red” and “blue”, respectively, under the assumption that the wavelength offsets are caused by Doppler redshifts and blueshifts. Table 3 includes the measured wavelengths and shifts for each of the observed lines. We observe blueshifts of 1500–2600 km s⁻¹ and redshifts of 800–1900 km s⁻¹. The FWHM line widths for both the red and the blue components are roughly 2500 km s⁻¹ for all lines. The equivalent widths for the integrated red+blue line pairs are 22.5 eV for Ne X, 17.8 eV for Ne IX, 24.6 eV for O VIII, and 44.4 eV for O VII.

3.4. Plasma Diagnostics

The relative strengths and shapes of the line components in a He-like triplet are a sensitive diagnostic of plasma temperature and density (Gabriel & Jordan 1973; Porquet & Dubau 2000). We denote the resonance, intercombination, and forbidden components as r , i , and f , respectively. We also denote hydrogenic Lyman α lines as h . Plasma temperature may be estimated from the ratio $G = (f + i)/r$. At high ($\gtrsim 10^6$ K) temperatures, there is an additional dependence on the ratio of hydrogenic and He-like ions, $H = h/r$. Plasma density may be inferred from the ratio $R = f/i$. We compute these ratios for each of our red and blue line components separately, and then compare them with the calculations of Porquet & Dubau (2000)

to infer plasma temperature and density. The results are summarized in Table 4.

We infer temperatures of $(1.6\text{--}1.8)\times 10^6$ K from the Ne IX lines and $(0.9\text{--}1.0)\times 10^6$ K from the O VII lines. For our density estimates, the R -value calculations of Porquet & Dubau were in fact made for temperatures close to these, although our R -values are low enough to be fairly insensitive to temperature in any case. The density of the Ne IX regions is about an order of magnitude higher than in the O VII regions.

Our observation of $r < i$ for the He-like lines would normally be interpreted as indicative of a purely photoionized plasma, in contrast to a hybrid plasma which experienced collisional ionization as well; however, this seems surprising for the high densities we measure. The calculations of Porquet and Dubau (2000) do not include scattering effects, which may be important in high-density regimes. From the fact that $G > 1$ is well established for all of our line components, we can deduce that the emission arises from a recombining plasma (A. Pradhan 2001, personal communication; Liedahl et al. 2001). Given that we observe moderately high densities in a hot recombining plasma, it seems likely that collisional ionization is indeed still important. The weak resonance line in the He-like triplets may therefore be an opacity effect due to enhanced line scattering.

TABLE 2
CONTINUUM SPECTRAL FITS

Model	N_{H} (10^{21} cm ⁻²)	Power law		Power law		Blackbody		χ^2_{ν}
		A_1^a	γ_1	A_2^a	γ_2	$R_{\text{km}}^2/D_{10\text{kpc}}^2$	kT (eV)	
PL+BB	0.26 ± 0.06	8.93 ± 0.14	0.84 ± 0.07	55.7 ± 25.1	333 ± 50	1.03
PL+BB	0.62 (fixed)	7.42 ± 0.14	0.65 (fixed)	173.0 ± 16.0	336 ± 42	1.05
PL+PL	0.87 ± 0.09	9.91 ± 0.41	0.84 ± 0.14	3.99 ± 0.64	2.51 ± 0.63	1.02
PL+PL	0.62 (fixed)	6.77 ± 0.84	0.65 (fixed)	5.87 ± 0.92	1.74 ± 0.30	1.06

^aNormalization of PL component at 1 keV in units of 10^{-3} erg cm⁻² s⁻¹ keV⁻¹.

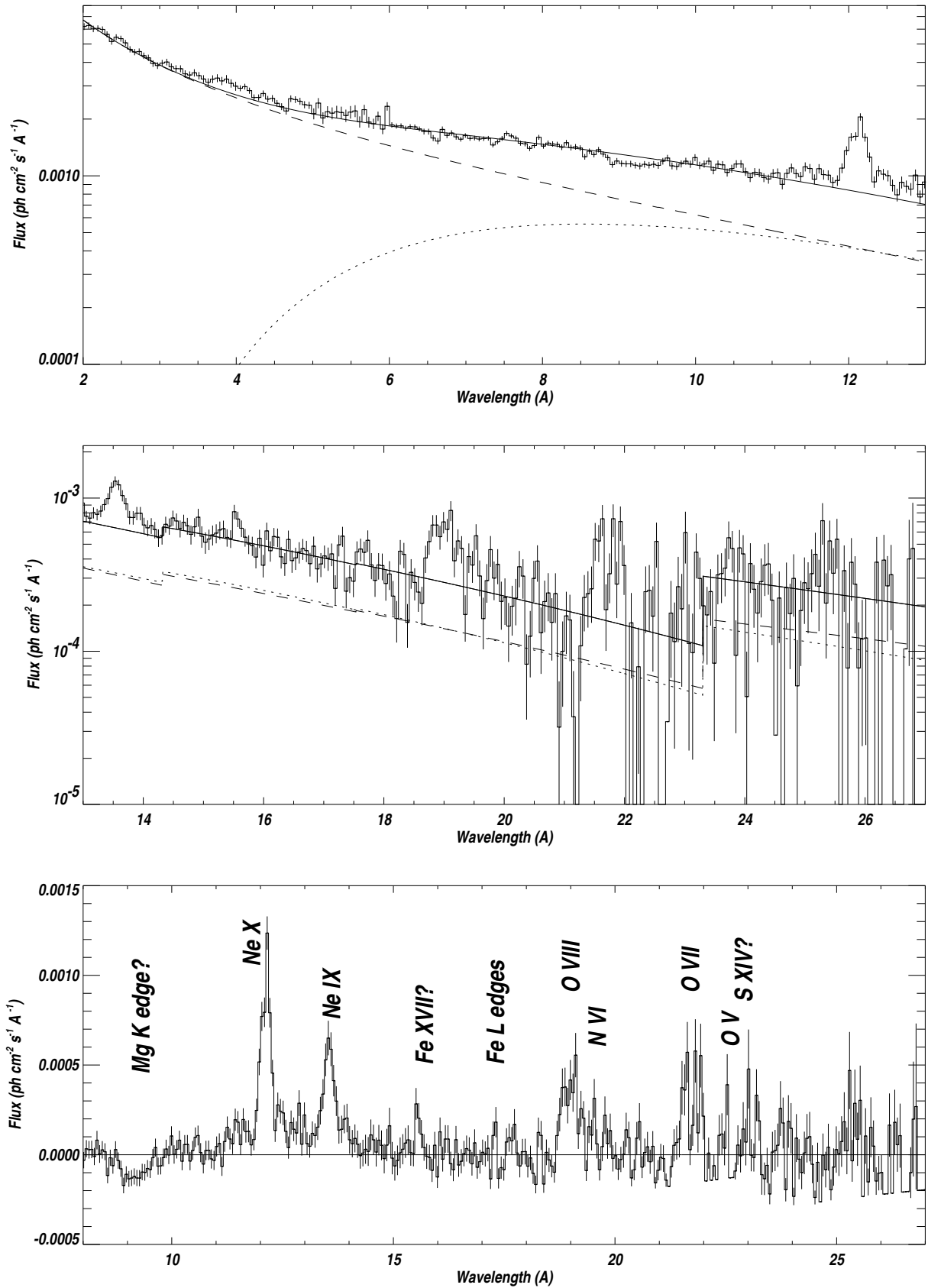


FIG. 3.— The HETGS photon spectrum of 4U 1626-67 as a function of wavelength, along with the best-fit power law (dashed line) and blackbody (dotted line) components. The residual spectrum in the bottom panel identifies various broad emission lines as well as ionization edges.

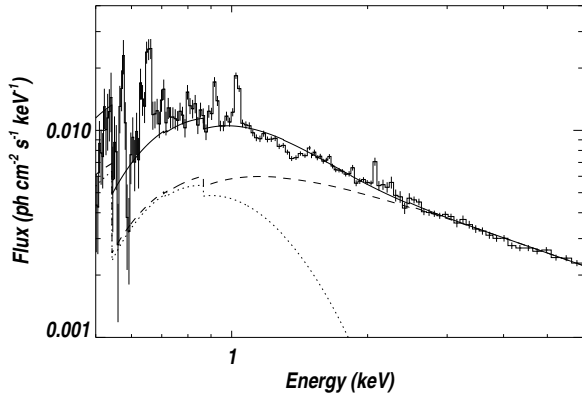


FIG. 4.— The broad-band photon spectrum of 4U 1626–67 as a function of energy, showing the relative contributions of the blackbody (dotted line) and power law (dashed line) components. The power law component clearly dominates at high energy.

This introduces some additional uncertainty to our measured G -value and the inferred temperature.

4. DISCUSSION

4.1. Origin of the Double-Peaked Emission Lines

We have resolved the previously detected Ne/O emission line complex into Doppler pairs of broadened lines from hydrogenic and He-like Ne and O. For most of the line pairs, the red and blue components have comparable strength (the one exception being the Ne X line). X-ray line complexes with well-separated red/blue line pairs have been previously detected from relativistic jets in the so-called Galactic microquasars SS 433 (Kotani et al. 1996; Marshall, Canizares, & Schulz 2001) and 1E 1740.1-2947 (Cui et al. 2000), but the Doppler shifts in those cases are relativistic, quite unlike what we observe in 4U 1626–67. Instead, the velocity width of the lines and their projected Doppler velocity shifts are of the same order of magnitude as the Keplerian velocities in the accretion disk (970 – 5400 km s $^{-1}$). Thus, the most natural explanation for these lines is that they arise in or near the Keplerian disk flow around the neutron star. Similar double line profiles are frequently observed in optical/UV emission lines from accretion disk flows in cataclysmic variables (see, e.g., Frank, King, & Raine 1992), but our observa-

tion would be the first X-ray detection of such features. (Single-peaked lines with comparable broadening and He-like line ratios have been observed in the edge-on LMXB EXO 0748–676; Cottam et al. 2001). We note that if this Keplerian explanation is correct, then the companion must be a $0.02 M_{\odot}$ white dwarf. The other alternative (a hydrogen-depleted, partially degenerate $0.08 M_{\odot}$ star) requires a very small ($\lesssim 8^{\circ}$) inclination. This gives a maximum projected velocity at the inner disk edge of only < 750 km s $^{-1}$, inconsistent with our observed Doppler shifts.

Alternatively, if the companion really is a more massive star, then we are viewing the disk nearly face-on and the Doppler line pairs are more difficult to understand. One possible explanation is that they arise in a bipolar outflow. Several authors have proposed that a magnetohydrodynamic wind might be driven from the magnetopause (near the inner disk edge) of an accreting neutron star during spin down (Anzer & Börner 1980; Arons et al. 1984; Lovelace, Romanova, & Bisnovatyi-Kogan 1995). Such an outflow would presumably have roughly the Keplerian velocity at the inner disk edge but would be oriented at a substantial angle to the disk plane. An advantage of this picture is that there is already indirect evidence that some outflow from the disk must be present, since the X-ray flux from the source (which traces \dot{M} onto the neutron star) has been steadily dropping for years while the optical flux (which traces \dot{M} through the disk) has remained unchanged. We can estimate the wind mass loss rate as $-\dot{M}_{\text{wind}} \sim A n_e m_p r^2 V \simeq 10^{-10} M_{\odot} \text{ yr}^{-1}$, where we have used the inner disk radius and Keplerian velocity and have taken $A = 16$ for oxygen. This is of the same order as the observed mass accretion rate onto the neutron star. However, a serious drawback of this explanation is that it fails to account for the comparable strengths of the red and blue line components, since we would expect the redshifted lines to be at least partially blocked from our line of sight by the accretion disk itself. Consequently, we do not regard this explanation as likely.

The He-like triplets of O and Ne are dominated by the intercombination component, indicating that the lines arise in a relatively dense, photoionized plasma (see, e.g., Liedahl et al. 2001). The inferred plasma temperatures (see Table 4) are considerably higher than the expected surface temperature range of the optically thick accretion disk. However, detailed calcu-

TABLE 3
EMISSION LINE PARAMETERS

λ^a (Å)	Ion	FWHM (km s $^{-1}$)	Blueshifted lines			Redshifted lines		
			Flux b	$\Delta\lambda^c$ (Å)	V (km s $^{-1}$)	Flux b	$\Delta\lambda^c$ (Å)	V (km s $^{-1}$)
12.130	Ne X	2860 ± 330	8.15 ± 0.93	-0.090 ± 0.014	-2220 ± 350	15.04 ± 1.65	0.050 ± 0.009	1240 ± 220
13.440	Ne IX (r)	2320 ± 300	1.68 ± 0.64	-0.070 ± 0.024	-1550 ± 530	1.91 ± 0.60	0.035 ± 0.013	770 ± 290
13.550	Ne IX (i)	2300 ± 290	5.19 ± 1.79	-0.070 ± 0.024	-1550 ± 530	5.41 ± 2.00	0.035 ± 0.013	770 ± 290
13.700	Ne IX (f)	2270 ± 280	1.69 ± 0.64	-0.070 ± 0.024	-1550 ± 530	1.92 ± 0.62	0.035 ± 0.013	770 ± 290
18.970	O VIII	3330 ± 380	14.04 ± 2.52	-0.110 ± 0.028	-1740 ± 440	17.82 ± 0.57	0.120 ± 0.030	1900 ± 480
21.600	O VII (r)	2430 ± 310	4.14 ± 1.84	-0.190 ± 0.073	-2610 ± 1000	5.26 ± 2.48	0.100 ± 0.041	1370 ± 560
21.800	O VII (i)	2410 ± 300	9.02 ± 3.64	-0.190 ± 0.073	-2610 ± 1000	9.59 ± 3.83	0.100 ± 0.041	1370 ± 560
22.100	O VII (f)	2380 ± 300	2.07 ± 1.03	-0.190 ± 0.073	-2610 ± 1000	1.88 ± 0.98	0.100 ± 0.041	1370 ± 560

^aCalculated values from Mewe et al. (1985).

^b 10^{-5} photons cm $^{-2}$ s $^{-1}$

^cMeasured shift from (a) in MEG.

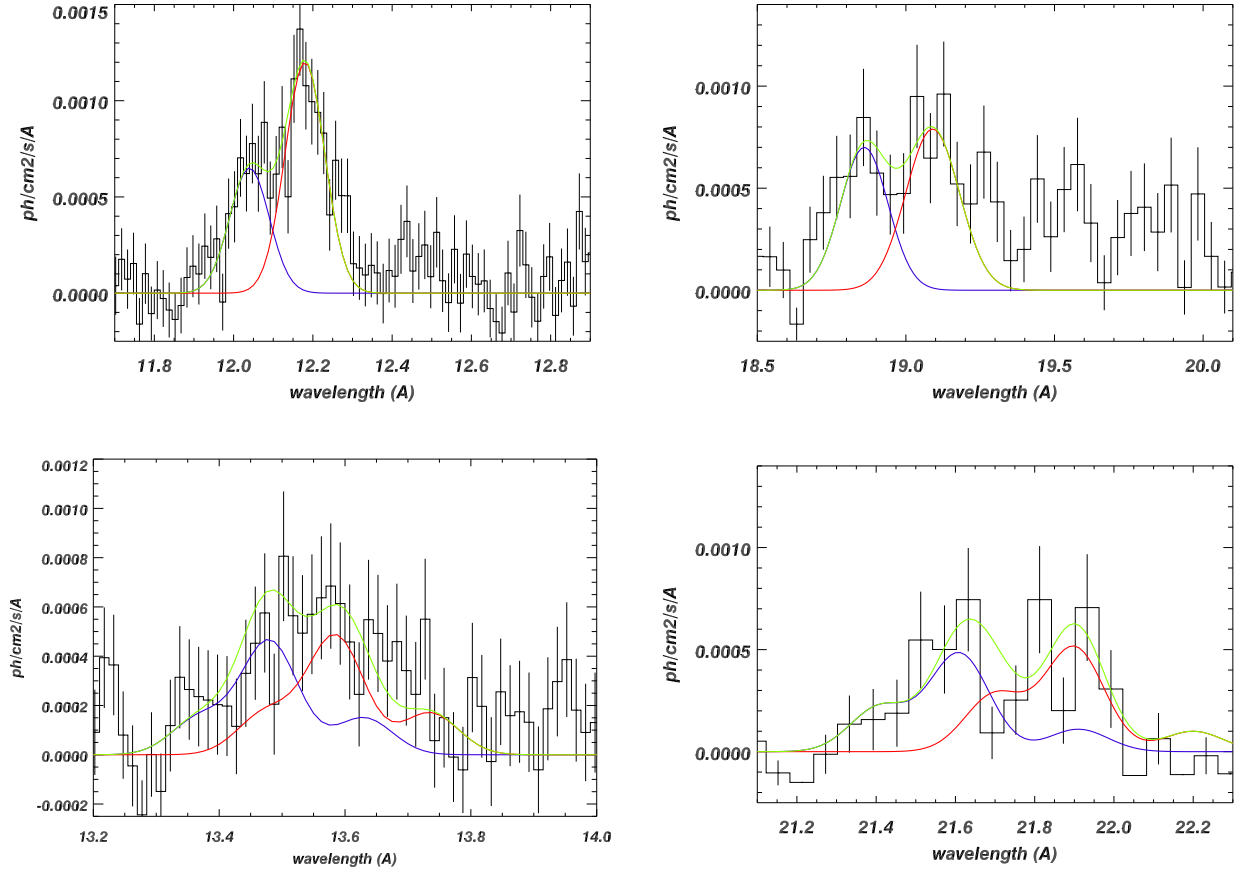


FIG. 5.— Double-peaked, broad emission lines from 4U 1626–67. The upper panels show the hydrogenic Ne X (*upper left*) and O VIII (*upper right*) lines, and the lower panels show the He-like triplets of Ne IX (*lower left*) and O VII (*lower right*). The blue curves denote the model for the blue-shifted components, the red curves the model for the red-shifted components, and the green curves the model for the overall line shape. In addition to the Doppler shifts, the individual line components are all broadened ($\approx 2500 \text{ km s}^{-1}$ FWHM).

lations of the structure of X-ray heated accretion disks indicate the existence of three sharply distinct layers near the surface: an X-ray heated, fully-ionized outer layer at the Compton temperature ($\sim 10^7\text{--}10^8 \text{ K}$); a thin, highly-ionized layer just below that, with $T \sim 10^6 \text{ K}$; and the usual, optically thick disk surface below that, with $T \sim 10^4\text{--}10^5 \text{ K}$ (Nayakshin, Kazanas, & Kallman 2000; Li, Gu, & Kahn 2001). Our measured temperatures and ionization states are thus consistent with those expected in the narrow, highly ionized layer just below the X-ray heated skin. For the observed O and Ne ion species to survive, the ionization parameter $\xi = L/nR^2$ must be below $10^3 \text{ erg cm}^{-2} \text{ s}^{-1}$ (Kallman & McCray 1982), where n is the ion number density. This gives a rough lower limit of $\gtrsim 1 \times 10^{10} d_{\text{kpc}} \text{ cm}$ for the radius of the line emitting region. This is consistent with an origin in the outer accretion disk, where X-ray heating effects dominate. We note that, for the inferred temperatures, plasma simulations with the XSTAR v2 code (Kallman & McCray 1982; Kallman & Bautista 2000) predict line emission from Si and S which we do not observe. This again points to an overabundance of Ne and O relative to solar values, as previously found by Angelini et al. (1995).

4.2. Absorption Edges and the Nature of the Mass Donor

Several of the observed photoelectric absorption edges are considerably stronger than expected for interstellar material, given the modest neutral hydrogen absorption determined from

$\text{Ly}\alpha$ measurements. We note that the most clearly detected strong edges are those of Ne and O, the same elements whose emission lines we discussed above. We thus conclude that the strong edges are due to absorption in cool, metal-rich material local to the source. (We may neglect local contributions to the hydrogen column density, as we know the donor in an ultracompact binary must be hydrogen-depleted; see Nelson et al. 1986.) Angelini et al. (1995) raised the possibility that 4U 1626–67 is embedded in the supernova remnant from the birth of the pulsar, but as they point out, the absence of strong lines from Si, S, and Fe is inconsistent with this idea. Instead, we presume that this cool material originated in the accretion disk or the mass donor, so that its composition is then a clue to the nature of the companion. In the last column of Table 1, we calculate the column density of material local to the source, assuming that the interstellar medium contributes $N_{\text{H}} = 4.5 \times 10^{20}$ with standard elemental abundances. The local column density of the element with atomic number Z is then $N_{\text{Z}}^{\text{loc}} = N_{\text{Z}}^{\text{tot}} - N_{\text{H}} A_{\text{Z}}$, where $N_{\text{Z}}^{\text{tot}}$ is the *total* measured column density of that element and A_{Z} is the number abundance of the element relative to hydrogen in the interstellar medium.

We may compare our resulting abundance ratios with those expected for the possible companion types. The Ne/O abundance ratio of 0.22 ± 0.15 is much larger than expected for either a partially degenerate hydrogen-depleted star or a He white dwarf. On the other hand, ^{22}Ne is the next most abundant ele-

TABLE 4
EMISSION LINE DIAGNOSTICS^a

Ion	H	G	R	T (10^6 K)	kT (eV)	n_e (10^{12} cm ⁻³)
Ne IX (blue)	4.85±0.73	4.10±0.62	0.33±0.08	1.62±0.65	140±56	8.3±1.4
Ne IX (red)	7.87±0.91	3.83±0.50	0.29±0.07	1.81±0.71	156±61	7.7±1.3
O VII (blue)	3.39±0.54	2.68±0.40	0.23±0.08	0.98±0.35	84±30	0.62±0.09
O VII (red)	3.39±0.54	2.18±0.35	0.20±0.08	0.91±0.65	78±56	0.85±0.12

^a $H = h/r$, $G = (f+i)/r$, and $R = f/i$, where r , i , and f are the fluxes of the resonance, intercombination, and forbidden components of the He-like triplet and h is the flux of the hydrogenic Ly α line.

ment in a C-O white dwarf, which has typical initial mass fractions of $X_C = X_O = 0.49$ and $X_{Ne} = 0.02$ (Segretain et al. 1994). This still gives a Ne/O ratio of only a few percent. However, a white dwarf that has cooled sufficiently will undergo crystallization (see, e.g., Shapiro & Teukolsky 1983), leading to chemical differentiation (Isern et al. 1991). In a C-O dwarf, this will cause all the Ne nuclei to settle into the inner few percent of the star and will also cause an O enhancement (Isern et al. 1991); detailed calculations predict $X_C \approx 0.19$, $X_O \approx 0.65$, and $X_{Ne} \approx 0.16$ (Segretain et al. 1994), consistent with our observed ratios. Note that since a mass of $0.02 M_\odot$ is required for a white dwarf secondary in this system, it is precisely the inner few percent of the star that is relevant, since the outer layers of the white dwarf would have been stripped away much earlier in the binary’s accretion history. The C/O abundance ratio is poorly constrained by our observations, but the range of allowed values is consistent with the expected ratio in the core of C-O dwarf that has crystallized.

If the feature near 9.5 \AA is in fact the Mg K -edge, then there is also a substantial overabundance of Mg relative to the solar value. The resulting Mg/O abundance ratio (0.17 ± 0.13) would be quite high for a C-O dwarf, and instead suggests the possibility that the companion is an O-Ne-Mg dwarf. Although these stars have a typical initial composition of $X_O = 0.72$, $X_{Ne} = 0.25$, and $X_{Mg} = 0.03$ (see Gutierrez et al. 1996 and references therein), crystallization during cooling would likely lead to a substantially enhanced central concentration of Mg, by analogy to what is calculated for C-O dwarfs (Ogata et al. 1993). Some models suggest that the central region might also contain some unburned ^{12}C from when the O-Ne-Mg dwarf is formed (Dominguez, Tornambe, & Isern 1994), which might account for the C overabundance suggested in our analysis.

Taken together, the double-peaked emission lines and strong absorption edges of Ne and O in our HETGS spectrum thus point to the companion in 4U 1626–67 being the chemically fractionated core of a C-O or O-Ne-Mg crystallized white dwarf, the first example of such a donor among the low-mass X-ray binaries. In either case, the progenitors of both components of the binary must have been massive stars in an initially wide orbit in order to avoid a common envelope phase prior to the formation of a C-O or O-Ne-Mg degenerate core (see

Levine et al. 1988 and references therein). The extremely low mass of the donor suggests an extended period of mass transfer. However, it is generally believed that prolonged mass transfer onto neutron stars leads to millisecond spin periods and weak ($\sim 10^8$ G) magnetic field strengths (e.g., Bhattacharya & van den Heuvel 1991). By contrast, 4U 1626–67 has a slow (7.66 s) spin period and a strong ($\sim 10^{12}$ G) magnetic field. One possible explanation is that the neutron star is relatively young and that it formed from accretion-induced collapse of a massive white dwarf (Taam & van den Heuvel 1986; Levine et al. 1988; Verbunt et al. 1990). If that is the case, then the strong absorption edges we observe may actually arise from material expelled from this progenitor at the time of its collapse into a neutron star, rather than from the mass donor or the accretion disk.

One further puzzle is to reconcile the observationally inferred mass transfer rate of $\dot{M} \approx 2 \times 10^{-10} M_\odot \text{ yr}^{-1}$ (Chakrabarty et al. 1997; Chakrabarty 1998; Wang & Chakrabarty 2001) with theoretical expectations. Mass transfer in a 42-min binary is driven by angular momentum losses via gravitational radiation (Verbunt & van den Heuvel 1995 and references therein). For a $0.02 M_\odot$ donor, we expect only $\dot{M} \approx 3 \times 10^{-11} M_\odot \text{ yr}^{-1}$. It is possible that the currently observed rate does not reflect the long-term average rate. Indeed, we note that for $\dot{M} \sim 10^{-11} M_\odot \text{ yr}^{-1}$, a C-O accretion disk may be subject to dwarf-nova-like thermal ionization instabilities (Menou, Perna, & Hernquist 2001). This may be true for O-Ne-Mg disks as well, although we are not aware of any explicit calculations. While 4U 1626–67 is generally considered a persistent source, its flux has been decaying steadily for over a decade. It is possible that it is actually a very long-lived X-ray transient, and that its average \dot{M} (calculated over many decades) is consistent with the theoretically predicted value.

It is a pleasure to thank Lars Bildsten for useful discussions, particularly on the subject of white dwarf composition and crystallization. The authors also thank the MIT HETG instrument team and the *Chandra* X-Ray Center for their support. This research was supported by contracts SAO SV1-61010 and NAS8-38249 as well as NASA grant NAG5-9184.

REFERENCES

- Angelini, L., White, N. E., Nagase, F., Kallman, T. R., Yoshida, A., Takeshima, T., Becker, C., & Paerels, F. 1995, *ApJ*, 449 L41
- Anzer, U. & Börner, G. 1980, *A&A*, 83, 133
- Arnaud, K. A. 1996, in *Astronomical Data Analysis Software and Systems V*, ed. G. Jacoby & J. Barnes (San Francisco: ASP Conf. Ser. 101), 17
- Arons, J., Burnard, D., Klein, R. I., McKee, C. F., Pudritz, R. E., & Lea, S. M. 1984, in *High Energy Transients in Astrophysics*, ed. S. E. Woosley (New York: AIP Press), 215
- Bhattacharya, D. & van den Heuvel, E. P. J. 1991, *Phys. Rep.*, 203, 1
- Chakrabarty D., 1998, *ApJ*, 492, 342
- Chakrabarty D. et al. 1997, *ApJ*, 474, 414
- Cottam, J., Kahn, S. M., Brinkman, A. C., den Herder, J. W., & Erd, C., 2001, *A&A*, 365, L277
- Cui, W., Schulz, N. S., Baganoff, F. K., Bautz, M. W., Doty, J. P., Garmire, G. P., Mirabel, I. F., Ricker, G. R., Rodríguez, L.F., & Taylor, S. C. 2001, *ApJ*, 548, 394
- Dominguez, I., Tornambe, A., & Isern, J. 1994, *ApJ*, 419, 268
- Elsner, R. F., Darbro, W., Leahy, D., Weisskopf, M. C., Sutherland, P. G., Kahn, S. M., & Grindlay, J. E. 1983, *ApJ*, 266, 769
- Frank, J., King, A., & Raine, D. 1992, *Accretion Power in Astrophysics*, 2nd ed. (Cambridge: Cambridge U. Press)
- Gabriel, A. H. & Jordan, C. 1973, *ApJ*, 186, 327
- Gutierrez, J., Garcia-Berro, E., Iben, I., Isern, J., Labay, J., & Canal, R. 1996, *ApJ*, 459, 701
- Isern, J., Mochkovitch, R., Garcia-Berro, E., & Hernanz, M. 1991, *A&A*, 241, L29
- Kallman, T. R. & Bautista, M. 2000, *BAAS*, 32, 1227 (HEAD abstract 27.03)
- Kallman, T. R. & McCray, R. 1982, *ApJS*, 50, 263
- Kii, T., Hayakawa, S., Nagase, F., Ikegami, T., & Kawai, N. 1986, *PASJ*, 38, 751
- Kortright, J. B. & Kim, S.-K. 2000, *Phys. Rev. B*, 62, 12216
- Kotani, T., Kawai, N., Matsuoka, M., & Brinkmann, W. 1996, *PASJ*, 48, 619
- Levine, A., Ma, C. P., McClintock, J., Rappaport, S., van der Klis, M., & Verbunt F. 1988, *ApJ*, 327, 732
- Li, Y., Gu, M. F., & Kahn, S. M. 2001, *ApJ*, submitted (astro-ph/0106163)
- Liedahl, A. D., Wojdowski P. S., Jimenez-Garate, M. A., & Sako, M. 2001, in *High-Resolution X-Ray Spectroscopy*, ed. G. Ferland (San Francisco: ASP Conf. Ser.), in press (astro-ph/0105084)
- Lovelace, R. V. E., Romanova, M. M., & Bisnovaty-Kogan, G. S. 1995, *MNRAS*, 275, 244
- Maurer, G. S., Johnson, W. N., Kurfess, J. D., & Strickman, M. S. 1982, *ApJ*, 254, 271
- Marshall, H. L., Canizares, C. R., & Schulz, N. S. 2001, *ApJ*, submitted
- Mavromatakis, F. 1994, *A&A*, 285, 503
- Menou, K., Perna, R., & Hernquist, L. 2001, *ApJ*, in press (astro-ph/0102478)
- Mewe, R., Gronenschild, E. H. B. M., & van den Oord, G. H. J. 1985, *A&AS*, 62, 197
- Middleditch, J., Mason, K. O., Nelson, J. E., & White, N. E. 1981, *ApJ*, 244, 1001
- Morrison, R. & McCammon, D. 1983, *ApJ*, 270, 119
- Nayakshin, S., Kazanas, D., & Kallman, T. R. 2000, *ApJ*, 537, 833
- Nelson, L.A., Rappaport, S. A., & Joss, P. C. 1986, *ApJ*, 304, 231
- Ogata, S., Iyetomi, H., Ichimaru, S., & van Horn, H. 1993, *Phys. Rev. E*, 48, 1344
- Orlandini, M., Dal Fiume, D., Frontera, F., del Sordo, S., Piraino, S., Santangelo, A., Segreto, A., Oosterbroek, T., & Parmar, A. N. 1998, *ApJ*, 500, L163
- Owens, A., Oosterbroek, T., & Parmar A. N. 1997, *A&A*, 324, L9
- Paczynski, B. & Sienkiewicz, R. 1981, *ApJ*, 248, 27
- Porquet, D. & Dubau, J. 2000, *A&AS*, 143, 495
- Pravdo, S. H. et al. 1979, *ApJ*, 231, 912
- Schulz, N. S., Cui, W., Canizares, C. R., Marshall, H. L., Lee, J. C., Miller, J. M., & Lewin, W. H. G. 2001, *ApJ*, in press (astro-ph/0109236)
- Segretain, L., Chabrier, G., Hernanz, M., Garcia-Berro, E., Isern, J., & Mochkovitch, R. 1994, *ApJ*, 434, 641
- Shapiro, S. L. & Teukolsky, S. A. 1983, *Black Holes, White Dwarfs, and Neutron Stars: The Physics of Compact Objects* (New York: Wiley)
- Taam, R. E. & van den Heuvel, E. P. J. 1986, *ApJ*, 305, 235
- Vaughan, B. A. & Kitamoto, S. 1997, preprint (astro-ph/9707105)
- Verbunt, F. & van den Heuvel, E. P. J. 1995, in *X-Ray Binaries*, ed. W. H. G. Lewin, J. van Paradijs, & E. P. J. van den Heuvel (Cambridge: Cambridge U. Press), 457
- Verbunt, F., Wijers, R. A. M. J., & Burm, H. M. G. 1990, *A&A*, 234, 195
- Verner, D. A., Yakovlev, D. G., Band, I. M., & Trzhaskovskaya, M. B. 1993, *Atomic Data & Nucl. Data Tables*, 55, 233
- Wang, Z. & Chakrabarty, D. 2001, *ApJ*, submitted